




Unraveling quantum pathways interference in two-color coherent control of photoemission with bias voltages

Yang Zhou  and Peng Zhang *

Department of Electrical and Computer Engineering, Michigan State University, East Lansing, Michigan 48824-1226, USA

 (Received 25 February 2022; revised 18 July 2022; accepted 20 July 2022; published 2 August 2022)

Coherent control steers a quantum system from an initial state to a target state by controlling quantum interference phenomena via an external field, which is central to vast applications ranging from quantum information processing to attosecond physics. Here, we analyze the quantum pathways interference in two-color coherent control of photoemission using exact analytical solutions of the time-dependent Schrödinger equation. The theory includes all possible quantum pathways and their interference terms. Constructive (or destructive) interferences among the pathways leads to the maximum (or minimum) emission with varying phase delay of the two-color lasers. It is found that increasing the intensity ratio of the second harmonic (2ω) to fundamental (ω) lasers results in less contribution from the ω pathway (absorption of ω photons only) and more contribution from multicolor pathway (simultaneous absorption of both ω and 2ω photons) and 2ω pathway (absorption of 2ω photons only), and therefore stronger pathways interference and increased visibility larger than 95%. Increasing bias voltages shifts the dominant emission to processes with lower-order photon absorption, which sequentially decreases the interference between the ω and the 2ω pathways, and between single-color and multicolor pathways, leading to two peaks in the visibility.

DOI: [10.1103/PhysRevB.106.085402](https://doi.org/10.1103/PhysRevB.106.085402)

I. INTRODUCTION

Coherent control of quantum systems relies on the manipulation of quantum interference phenomena via external fields such as laser pulses. Two-color laser field consisting of a strong fundamental laser and a weak second harmonic has become an essential tool to probe and steer quantum pathways interference in the interaction with matter. Recently, two-color coherent control of photoemission from nanotips has drawn great interest, for its flexibility in manipulating electron dynamics in ultrashort temporal scale and nanometer spatial scale [1–6], which makes it applicable in spatiotemporal characterization of surface plasmon polaritons [7–9], investigation of hot-carrier dynamics [2], and strong-field photoemission [10,11], and control of interference fringes in the momentum distribution of electron emission [12,13]. It also opens up new opportunities in flexible control of photoemission in applications such as time-resolved electron microscopy [14–17], free-electron lasers [18,19], carrier-envelope phase detection [20–22], and emerging nanophotonic and nanoelectronic devices [23–28].

By tuning the intensity mixture ratio and relative phase difference between the fundamental laser and its second harmonic, the photoemission current can be modulated with a contrast of up to 97.5% [3,5,6,29–31]. The strong modulation of photoemission current by two-color laser is ascribed to the quantum interference between competing pathways. The excitation of two-color laser opens out multicolor quantum pathways where photons of different colors are simultaneously absorbed. Depending on the two-color intensity mixture

ratio, simple two-pathway or three-pathway quantum interference model has been used to explain the scaling of the coherent signal to the second-harmonic intensity in experiments [3,29,31,32]. However, to give satisfactory fitting to the experimental results, the simple quantum pathway model has to be modified to allow independent weights for the three channels and to account for the discrepancy in the extracted prefactors from those of independent pulses [32]. As another key tuning knob, increasing DC bias field enhances electron emission but meanwhile suppresses the current modulation, as experimentally observed in Refs. [29,32]. Nevertheless, how the DC bias field influences the weight of each pathway and interference between them is still ambiguous. Analyzing the quantum pathway model using exact quantum theory is therefore of highest interest for photoemission from metals in two-color fields and for coherent control schemes in general [32].

In this work, we analyze the quantum pathways interference with the exact analytical solutions of the time-dependent Schrödinger equation (TDSE) including DC bias [5,6]. These exact analytical quantum models for two-color laser-induced photoemission show quantitative good agreement with experimental results [5,6] and demonstrate the potential in measurement of time-resolved photoelectron energy spectra [6,33]. Our analysis explicitly shows the effects of laser fields and DC bias field on the weights of each pathway and the interference effects among them.

II. RESULTS

The one-dimensional (1D) model is illustrated in Fig. 1(a). Electrons with initial energy of ε emit through the metal-vacuum interface ($x = 0$) due to DC field F_0 and two-

*pz@egr.msu.edu

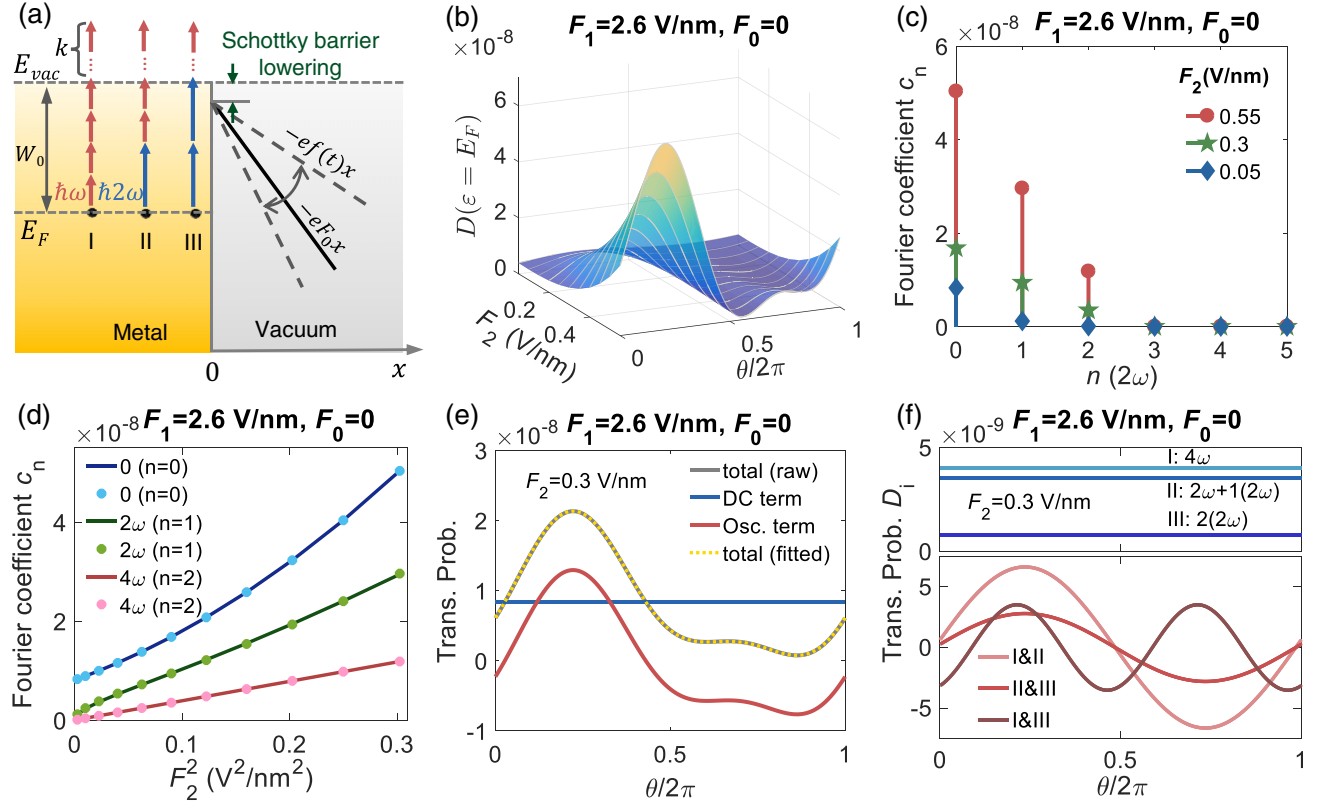


FIG. 1. (a) Energy diagram for photoemission from a metal surface induced by two-color laser fields $f(t) = F_1 \cos(\omega t) + F_2 \cos(2\omega t + \theta)$ under a DC field F_0 . Red and blue arrows depict quantum pathway model, with pathway I: absorption of $(4 + k)$ fundamental photons (red arrow); pathway II: absorption of $(2 + k)$ fundamental photons and 1 second-harmonic photon (blue arrow); pathway III: absorption of 2 second-harmonic photons and k fundamental photons. (b) Electron transmission probability from initial energy $\varepsilon = E_F$, $D(\varepsilon = E_F)$, as a function of 2ω laser field F_2 and phase delay θ , with $F_1 = 2.6$ V/nm and $F_0 = 0$. (c) Coefficients of Fourier series expansion for $D(\tau)$ for $F_2 = 0.05, 0.3$, and 0.55 V/nm. (d) Fourier series coefficients at angular frequency of 0 ($n = 0$), 2ω ($n = 1$), and 4ω ($n = 2$) as a function of F_2^2 . Scatters represent coefficients from Fourier series expansion of $D(\tau)$ from the exact quantum model in Eqs. (2) and (3), and solid curves are fitted from the quantum pathway model in Eq. (4). (e) Decomposed electron transmission probability, with blue curves the zero-frequency terms and red curves the oscillatory terms (2ω and 4ω terms). (f) Electron transmission D_i through each quantum pathway (top) and their interference terms (bottom).

color laser field $f(t) = F_1 \cos \omega t + F_2 \cos(2\omega t + \theta)$, where F_1 and F_2 are the magnitudes of the fundamental and second-harmonic electric fields, respectively, ω is the angular frequency of the fundamental laser, $\theta = 2\omega\tau$ is the relative phase between the fundamental and second harmonic, with τ the corresponding time delay. For simplicity, the fields are assumed to be perpendicular to the metal surface and abruptly cut off inside the metal [5,6,22,34]. The potential barrier seen by electrons inside the metal reads

$$\phi(x, t) = \begin{cases} 0, & x < 0 \\ V_0 - ef(t)x - eF_0x, & x \geq 0 \end{cases}, \quad (1)$$

where $V_0 = E_F + W_{\text{eff}}$, E_F is the Fermi energy of the metal, and $W_{\text{eff}} = W_0 - W_{\text{Schottky}}$ is the effective work function with W_0 the nominal work function and $W_{\text{Schottky}} = 2\sqrt{e^3 F_0 / 16\pi \varepsilon_0}$ the Schottky barrier lowering due to DC field F_0 , e (>0) is the elementary charge, and ε_0 is the vacuum permittivity. By exactly solving TDSE subject to the potential barrier in Eq. (1), the time-averaged electron transmission probability

from energy level ε is obtained as [5,6]

$$D(\varepsilon) = \sum_{l=-\infty}^{\infty} w_l(\varepsilon), \quad (2)$$

where $w_l(\varepsilon)$ represents the electron emission through l -photon processes, with $l < 0$ being multiphoton emission, $l = 0$ direct tunneling, and $l > 0$ multiphoton absorption processes [5,6,33–36]. The expression of w_l is summarized in the Appendix. More detailed derivation can be found in Ref. [5] for $F_0 = 0$ and in Ref. [6] for $F_0 \neq 0$. It is important to note that although l in Eq. (2), as written, is referred to the number of fundamental photons $\hbar\omega$, it also includes the possible processes of substituting two fundamental photons $2\hbar\omega$ with a single second-harmonic photon $\hbar(2\omega)$, illustrated in the three possible pathways in Fig. 1(a), as well as arbitrary multiples of such substitutions.

Figure 1(b) shows the electron emission probability from Fermi level $D(\varepsilon = E_F)$ as a function of second-harmonic laser field F_2 and relative phase θ , with fundamental laser field $F_1 = 2.6$ V/nm and DC field $F_0 = 0$. The metal is assumed as gold, with $W_0 = 5.1$ eV and $E_F = 5.53$ eV. The fundamental laser has the wavelength of 800 nm (photon energy of 1.55 eV). For

a given F_2 , $D(\varepsilon = E_F)$ is a periodic function of relative phase θ with an angular frequency of 2ω . Maxima of $D(\varepsilon = E_F)$ for a given F_2 are observed at $\theta \cong \pi/2$ (see Fig. S1(a) in Supplemental Material [37]), whereas the minima are at $\theta \cong 3\pi/2$ when $F_2 \leq 0.4$ V/nm and at $\theta \approx \pi$ when $F_2 > 0.4$ V/nm. Visibility or the modulation depth due to relative phase θ , which is defined as the ratio of the difference between the maximum and the minimum of transmission probability in θ domain to the summation of them, increases as F_2 increases for $F_2 \leq 0.3$ V/nm and keeps almost constant for $F_2 > 0.3$ V/nm (see Fig. S1(b) in Supplemental Material [37]).

Figure 1(c) shows the Fourier series coefficient c_n of $D(\varepsilon = E_F)$ vs τ at multiples of second-harmonic laser frequency 2ω , obtained from

$$D(\tau) = \frac{c_0}{2} + \sum_{n=1}^N c_n \sin[n(2\omega)\tau + \varphi_n], \quad (3)$$

$$D_I \propto \alpha^k (F_1^2)^k [\alpha^4 (F_1^2)^4] = K_I, \quad (4a)$$

$$D_{II} \propto \alpha^k (F_1^2)^k [\zeta^2 (F_1^2)^2 F_2^2] = K_{II} F_2^2, \quad (4b)$$

$$D_{III} \propto \alpha^k (F_1^2)^k [\beta^2 (F_2^2)^2] = K_{III} (F_2^2)^2, \quad (4c)$$

$$D_{I\&II} \propto 2\sqrt{D_I D_{II}} \cos \theta \propto \alpha^k (F_1^2)^k [2\alpha^2 \zeta (F_1^2)^3 \sqrt{F_2^2} \cos \theta] = K_{I\&II} \sqrt{F_2^2} \cos(2\omega\tau), \quad (4d)$$

$$D_{I\&III} \propto 2\sqrt{D_I D_{III}} \cos 2\theta \propto \alpha^k (F_1^2)^k [2\alpha^2 (F_1^2)^2 \beta F_2^2 \cos 2\theta] = K_{I\&III} F_2^2 \cos(4\omega\tau), \quad (4e)$$

$$D_{II\&III} \propto 2\sqrt{D_{II} D_{III}} \cos \theta \propto \alpha^k (F_1^2)^k [2\zeta F_1^2 \beta \sqrt{(F_2^2)^3} \cos \theta] = K_{II\&III} \sqrt{(F_2^2)^3} \cos(2\omega\tau), \quad (4f)$$

where α , ζ , and β are the weights for pathways I, II, and III, respectively, and K_i is the prefactor for each term as a power function of F_2^2 . Equating the total transmission probability $D(\tau)$ in Eq. (3) with the sum of all the probabilities in Eqs. (4a)–(4f) enables us to extract straightforwardly the weights α , ζ , and β from the Fourier coefficients.

By setting $k = 0$ (see Fig. S2 for fitting K_i s as a function of F_1^2 in Supplemental Material [37]), the fitted K_I , K_{II} , and K_{III} in Fig. 1(d) yield $\alpha = 1.18 \times 10^{-3} \text{nm}^2/\text{V}^2$, $\zeta = 2.93 \times 10^{-5} \text{nm}^3/\text{V}^3$, and $\beta = 3.17 \times 10^{-4} \text{nm}^2/\text{V}^2$. With these K_i weights [Fig. 1(d)], the transmission probability $D(\varepsilon = E_F)$ is decomposed into a DC term (zero-frequency term) and an oscillatory term (consisting of 2ω and 4ω terms), as exemplified in Fig. 1(e) for $F_2 = 0.3$ V/nm. Fourier series expansion with these fitting parameters perfectly reproduces the raw data from our quantum model obtained from Eq. (2).

Photoemission through each of the channels in Eq. (4) is explicitly shown in Fig. 1(f). It is clear that pathways I and II in combination form the majority of the constant baseline emission channels, around which the transmission probability oscillates with the relative phase θ . The strongest interference is between pathways I and II. Interference terms, and therefore the total transmission probability, can be strongly tuned by the phase difference θ , with maximum at $\theta \cong \pi/2$ and minimum at $\theta \cong 1.8\pi$, as shown in Figs. 1(e) and 1(f).

with $c_0 = \frac{2}{T} \int_0^T D(\tau) d\tau$, $c_n = \sqrt{a_n^2 + b_n^2}$, $a_n = \frac{2}{T} \int_0^T D(\tau) \cos(n(2\omega)\tau) d\tau$, $b_n = \frac{2}{T} \int_0^T D(\tau) \sin[n(2\omega)\tau] d\tau$, $T = \frac{2\pi}{2\omega}$, and $\varphi_n = \tan^{-1}(\frac{a_n}{b_n})$. Three dominant components at angular frequencies of 0 , 2ω , and 4ω are observed for $F_2 = 0.05$, 0.3 , and 0.55 V/nm. As F_2 increases, c_1 and c_2 increase and their relative differences to c_0 become smaller, indicating more contribution from high-frequency components.

These Fourier coefficients are shown as a function of F_2^2 as scatters in Fig. 1(d). The results are fitted with the quantum interference model [3,29,31,32], which considers pathways I, II, and III as illustrated in Fig. 1(a), with the red and blue arrows representing absorption of one fundamental photon and one second-harmonic photon, respectively. The transmission probabilities of each pathway and of the interference terms between them are

The effect of second-harmonic laser field F_2 on the contribution of each channel to the total emission is shown in Fig. 2. Transmission probability D_i through each channel i at the maximum of total $D(\varepsilon = E_F)$ in θ domain for a given F_2 is plotted in Fig. 2(a). The corresponding normalized transmission probability with respect to the total $D(\varepsilon = E_F)$ is shown in Fig. 2(b). When $F_2 \lesssim 0.2$ V/nm, pathway I and the interference of I&II account for more than 66% of the total emission, whereas contribution from pathway III can be neglected. The negligibility of pathway III for a low field mixture ratio ($F_2/F_1 < 7\%$ here) is further confirmed by the visibility analysis (see Fig. S1(b) in Supplemental Material [37]), which is consistent with previous work for tungsten [3]. As F_2 increases, transmission probability through all channels except pathway I increases, exhibiting strong constructive interferences from I&II, II&III, and I&III. When $F_2 \gtrsim 0.35$ V/nm, contributions from channels II, I&III, and II&III exceed that from pathway I. The interference II&III surpasses I&II at $F_2 \cong 0.46$ V/nm. Figures 2(c) and 2(d) show the transmission probability and their normalized value at minima of $D(\varepsilon = E_F)$ in θ domain as a function of F_2 . The interference terms I&II, II&III, and I&III are negative, which indicate destructive interferences and greatly suppress the total transmission probability. More details of the effect of F_2 are given by analyzing the dependence of $D_i(\varepsilon = E_F)$ vs τ for $F_2 = 0.05$, 0.3 , and 0.55 V/nm in Fig. S3 in Supplemental

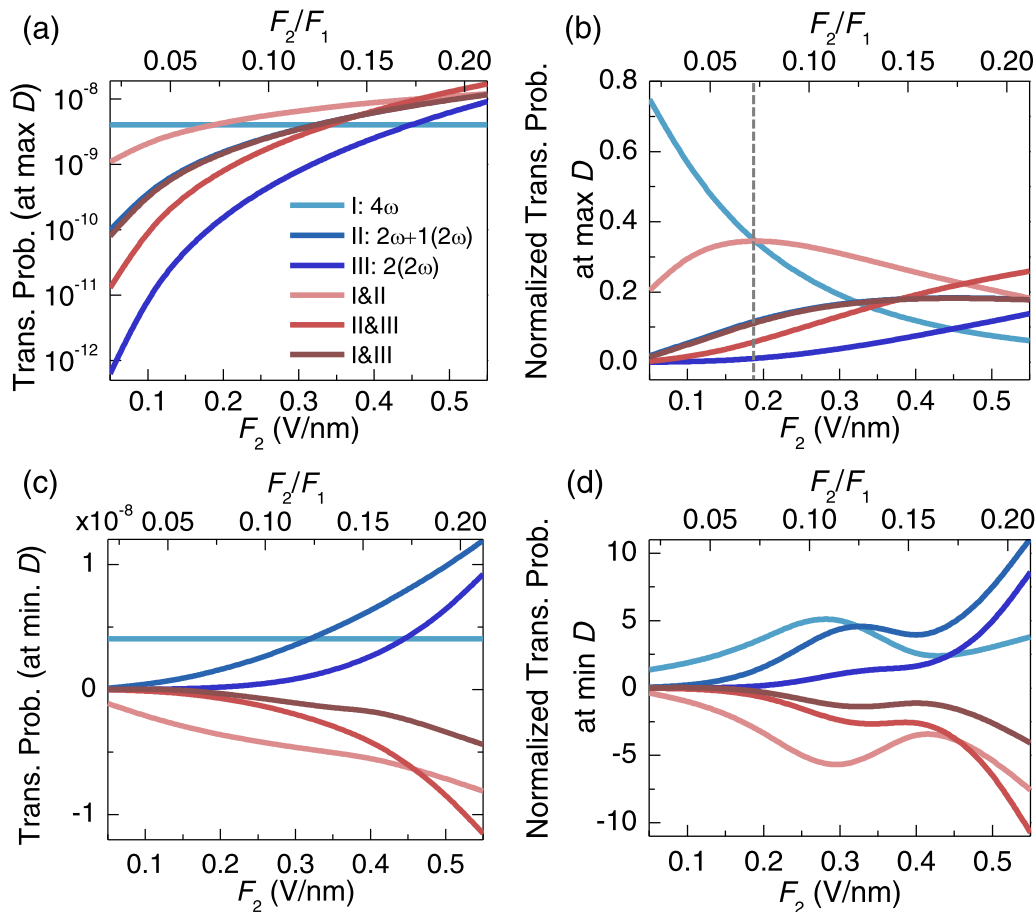


FIG. 2. (a) Electron transmission probability D_i through each channel and (b) the corresponding normalized transmission probability D_i/D at maximum of $D(\varepsilon = E_F)$ in θ domain for a given F_2 . (c) D_i and (d) D_i/D at minimum of $D(\varepsilon = E_F)$ in θ domain for a given F_2 . Here, $F_1 = 2.6$ V/nm and $F_0 = 0$.

Material [37], which reconfirms the above observation. When F_2 increases to 0.55 V/nm, emission through pathway II and interference II&III become the dominant DC and oscillatory terms, respectively.

Figure 3 shows the effect of fundamental laser field on the modulation of quantum interference and the contribution of each pathway. As shown in Fig. 3(a), when F_1 increases, the visibility increases and then decreases, with the maximum at $F_1 = 2.6$ V/nm, corresponding to the intensity ratio of second harmonic to the fundamental of 1.3%, with fixed second-harmonic field $F_2 = 0.3$ V/nm and DC field $F_0 = 0$. The transmission probability from initial energy level $\varepsilon = E_F$ as a function of relative phase θ is shown as inset in Fig. 3(a) under various fundamental laser fields F_1 . As F_1 increases, $D(\varepsilon = E_F)$ is greatly enhanced. The oscillation magnitude gradually decreases for $F_1 > 2.6$ V/nm, consistent with the decreasing visibility in Fig. 3(a).

The decrease of the visibility is ascribed to smaller two-color laser intensity ratio, which results in relatively less contribution from pathways II and III and therefore the interference terms, as shown in Fig. 3(b). When $F_1 < 2$ V/nm (or $F_2/F_1 > 0.15$), the dominant emission is through pathway III and the interference term II&III. As F_1 increases, electron emission through pathway I and interference I&II increases greatly. As F_1 reaches ~ 3.7 V/nm, the contribution from

pathway I exceeds that of the interference term I&II. For $F_1 > 3.7$ V/nm, while I&II remains the dominant interference term, its contribution to photoemission continues to decrease.

As another key knob to the coherent control of electron emission by two-color lasers, the effect of DC field is shown in Fig. 4. In Fig. 4(a), $D(\varepsilon = E_F)$ is plotted as a function of relative phase θ under various DC fields F_0 . As F_0 increases, transmission probability is greatly enhanced due to the lowering and narrowing of the surface potential barrier, which opens emission channels of lower order (cf. Fig. 2 in Ref. [6]). The minimum shifts from $\theta \cong 1.7\pi$ to $\theta \cong \pi$, which indicates the suppression of high-order 4ω terms. Figure 4(b) shows the visibility as a function of F_0 under different second-harmonic laser fields with $F_1 = 2.6$ V/nm. For $F_2 \leq 0.3$ V/nm, the maximum visibility is observed at $F_0 \cong 0.5$ V/nm, whereas for $F_2 \geq 0.4$ V/nm, the maximum occurs at $F_0 = 0$. Another peak also appears at $F_0 \cong 1.75$ V/nm for all cases. When $F_0 > 1.75$ V/nm, visibility decreases. As F_0 reaches 3 V/nm, visibility drops to almost 0 for all cases.

The nonlinear dependence of visibility on DC fields can be explained by looking at the Fourier series coefficient, as shown in logarithm scale in Fig. 4(c). When $F_0 \geq 0.5$ V/nm, the high-frequency component at 4ω is suppressed compared to the 0 and 2ω terms. As F_0 further increases, the difference between the coefficient at zero frequency and that at

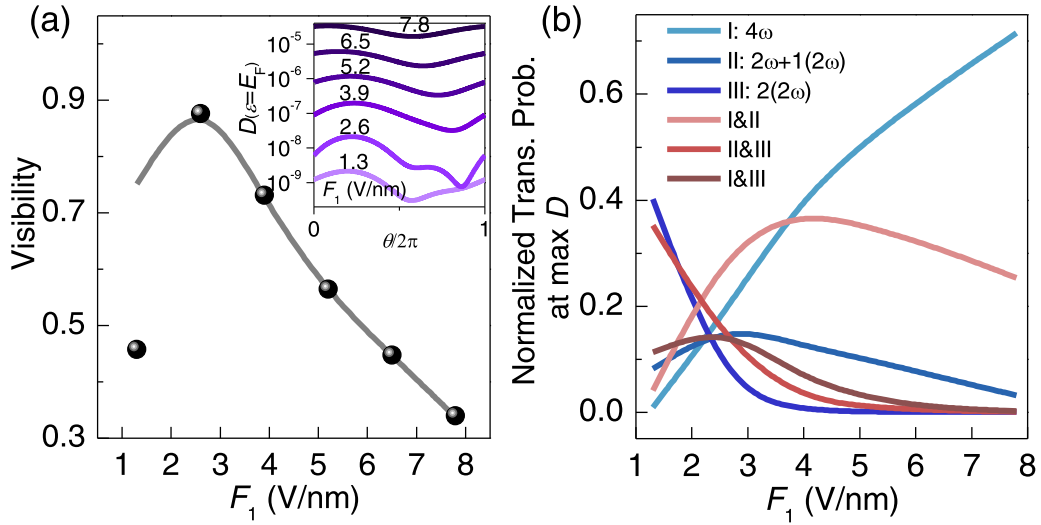


FIG. 3. (a) Visibility as a function of F_1 . Gray solid curve: calculated directly from the data by the quantum model in Eq. (2); black scatters: calculated from visibility = $D_{I\&II}/(D_I + D_{II})$ with D_I , D_{II} , and $D_{I\&II}$ from Eq. (4) using fitted parameters; inset: transmission probability as a function of relative phase under different F_1 . (b) Normalized transmission probability over the total transmission probability at maximum of $D(\varepsilon = E_F)$ in θ domain as a function of F_1 . Here, we fix $F_2 = 0.3$ V/nm and $F_0 = 0$.

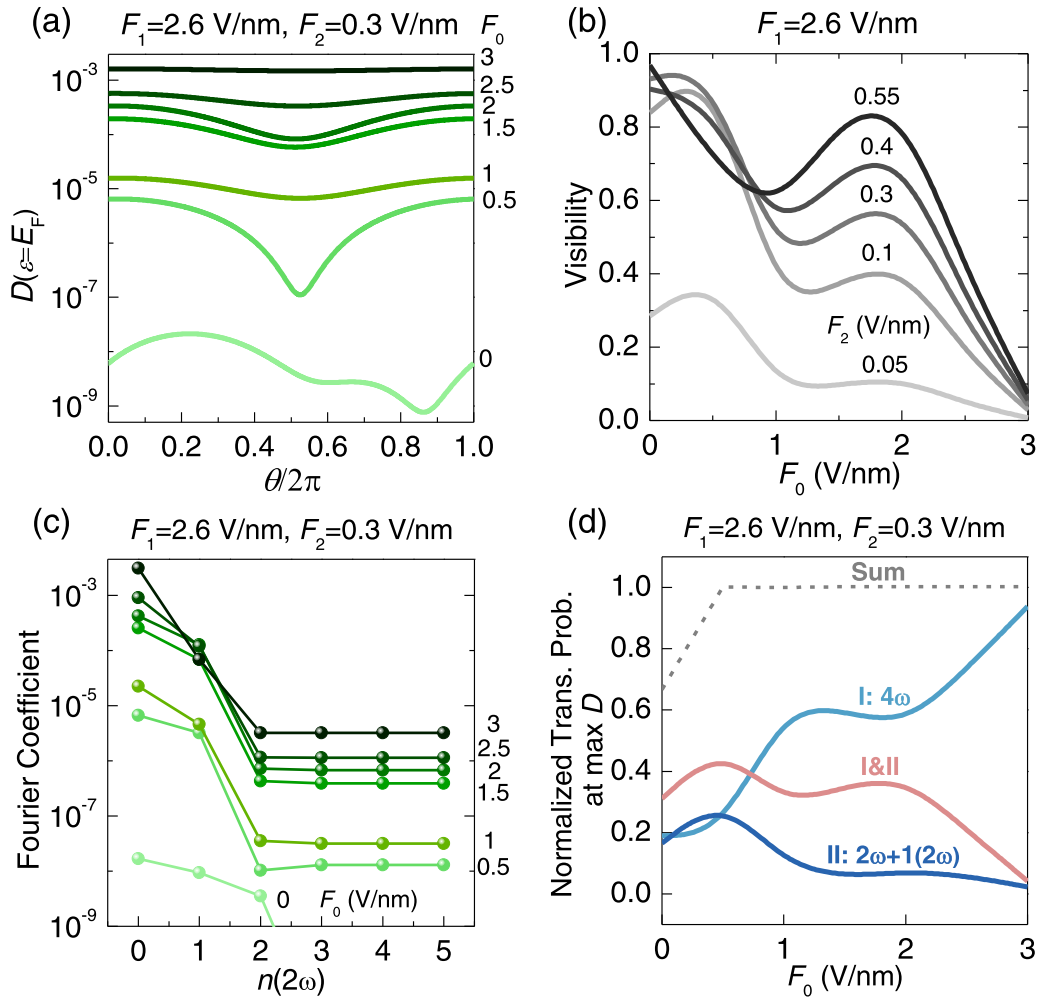


FIG. 4. (a) $D(\varepsilon = E_F)$ as a function of phase delay θ under various DC fields F_0 . (b) Visibility as a function of F_0 under various F_2 . (c) Fourier series coefficients under various F_0 . (d) Normalized transmission probability over the total transmission probability at maximum of $D(\varepsilon = E_F)$ in θ domain as a function of F_0 . Here, we use $F_1 = 2.6$ V/nm and $F_2 = 0.3$ V/nm in (a), (c), and (d).

2ω increases. When F_0 is sufficiently large, the component at 2ω becomes also negligibly small compared to the zero-frequency component. Thus, the peaks around 0–0.5 V/nm and 1.75 V/nm in Fig. 4(b) can be attributed to the 4ω and 2ω components, respectively. Note the peaks are also observed in previous experiments (inset in Fig. 5 of Ref. [32]). Normalized transmission probability at maximum of $D(\varepsilon = E_F)$ in the θ domain in Fig. 4(d) also confirms this observation. Since the 4ω term is negligible for the majority of the cases, only pathways I, II, and their interference I&II are considered here for simplicity. When $F_0 < 0.5$ V/nm, those two pathways and the interference between them cannot account for the total emission, as the sum of those terms is smaller than 1, indicating additional contributions from the 4ω term are needed in this regime. As $F_0 \geq 0.5$ V/nm, the sum approaches 1. The contribution from pathway I to the total emission increases, while the contribution from the other two channels decreases. It is important to note that, different from the physical meaning of absorption of 4 photons of fundamental laser in the absence of DC field, pathway I with positive F_0 also includes contributions from direct tunneling, photon-assisted tunneling, and photon-emission tunneling (cf. Fig. 2 in Ref. [6]), which are all captured by the prefactors with power of k in Eq. (4).

III. CONCLUSION

In conclusion, we analyze quantum pathways interference in two-color coherent control of photoemission using exact analytical solutions of the TDSE including DC bias. The exact theory includes the contribution from all possible quantum pathways and their interference terms. Interference among pathways physically explains the observed modulation of photoemission current by the relative phase between two-color lasers. Effects of two-color laser fields and DC bias field on the weights of each pathway and interference between them are explicitly demonstrated. It is found that increasing the intensity ratio of the second harmonic to fundamental lasers would result in more contribution from multicolor pathway and the single-color pathway of absorption of 2ω photons, and therefore stronger interference between them and increased visibility more than 95%. Increasing bias voltages opens out lower photon order channels including photoassisted tunneling and direct tunneling, which inhibits contribution from both single-color and multicolor multiphoton absorption. Implied by the quantum pathways interference model is that the lower-order photon-assisted and direct tunneling processes are also incorporated in the different pathways with the presence of the DC bias. As a result, interferences through different pathways are sequentially decreased with the increase of DC bias voltage, leading to the subsequent suppression of 4ω and then 2ω components in the Fourier analysis of current modulation with respect to the relative phase between the two-color lasers. This helps explain the two peaks in the visibility as a function of bias voltage.

Our study provides direct theoretical foundation to confirm the coherent emission physics of replacing two fundamental photons with one second-harmonic photon despite various possible pathways. Our quantum theory and the

corresponding pathways model are applicable to arbitrary driving-laser frequency, intensity (below the material damage threshold), and material properties. Our study provides insights into two-color laser-induced photoelectron emission dynamics and more general coherent control schemes of quantum systems ranging from single atoms and molecules [38,39], nano-objects [8,40], and material surfaces and interfaces [26,41–44]. Manipulating ionization pathways and the corresponding quantum phases between pathways enable us to develop methods for controlling excitation and ionization processes in atoms, molecules, and materials under strong laser fields [45–49]. Therefore, identifying and quantifying quantum pathways and corresponding quantum phases are fundamentally important to both the understanding of the photoionization dynamics and the characterization of the atomic and molecular structures. Our analysis using the exact analytical quantum model in combination with the Fourier analysis can provide a systematic investigation into the parametric dependence of each pathway as well as interference terms among them. The parametric scaling of different pathways would be helpful in the optimization of the input laser parameters to achieve coherent control through a specific pathway in a given quantum system.

ACKNOWLEDGMENTS

This work was supported by the Air Force Office of Scientific Research (AFOSR) YIP Award No. FA9550-18-1-0061 and the Office of Naval Research (ONR) YIP Grant No. N00014-20-1-2681.

APPENDIX

For completeness, we provide the expression for the key results of our quantum model developed in Refs. [5,6]. More details about the derivation of these results can be found in Refs. [5] and [6]. With the assumptions listed in the main text, the electron wave function $\psi(x, t)$ is solved exactly from the 1D time-dependent Schrödinger equation:

$$i\hbar \frac{\partial \psi(x, t)}{\partial t} = -\frac{\hbar^2}{2m} \frac{\partial^2 \psi(x, t)}{\partial x^2} + \phi(x, t)\psi(x, t), \quad (\text{A1})$$

where \hbar is the reduced Planck constant, m is the electron mass, x is the distance to the metal surface, and $\phi(x, t)$ is the potential barrier given in Eq. (1) in the main text.

The exact analytical solution for electron waves inside the metal ($x < 0$) is

$$\psi_l(x, t) = \exp\left(-i\frac{\varepsilon}{\hbar}t + ik_0x\right) + \sum_{l=-\infty}^{\infty} R_l \times \exp\left(-i\frac{\varepsilon + l\hbar\omega}{\hbar}t - ik_lx\right), \quad x < 0, \quad (\text{A2})$$

where ε is the electron initial energy, $k_0 = \sqrt{2m\varepsilon/\hbar^2}$ and $k_l = \sqrt{2m(\varepsilon + l\hbar\omega)/\hbar^2}$ are the electron wave numbers, and R_l is the reflection coefficient of the incident electron wave after l -photon process.

The exact analytical solution for the transmitted electron wave outside the metal ($x \geq 0$) is obtained using Truscott transformations [5,6,50] from Eq. (A1) and separation of variables, which reads

$$\begin{aligned} \psi_{II}(x, t) = & \sum_{l=-\infty}^{\infty} T_l \exp \left[i \sqrt{\frac{2mE_l}{\hbar^2}} \left(x + \frac{eF_1 \cos \omega t}{m\omega^2} + \frac{eF_2 \cos(2\omega t + \theta)}{4m\omega^2} \right) \right] \\ & \times \exp \left[-i \frac{\varepsilon + l\hbar\omega}{\hbar} t + i \frac{x}{\hbar} L + i \frac{e^2}{8\hbar m \omega^3} M - i \frac{e^2 F_1 F_2}{4\hbar m \omega^2} N \right], \quad x \geq 0, \end{aligned} \quad (\text{A3a})$$

when $F_0 = 0$, and

$$\begin{aligned} \psi_{II}(x, t) = & \sum_{l=-\infty}^{\infty} T_l [Ai(-\eta_l) - iBi(-\eta_l)] \exp \left[-i \frac{e^2 F_0 F_1 \sin \omega t}{\hbar m \omega^3} - i \frac{e^2 F_0 F_2 \sin(2\omega t + \theta)}{8\hbar m \omega^3} \right] \\ & \times \exp \left[-i \frac{\varepsilon + l\hbar\omega}{\hbar} t + i \frac{x}{\hbar} L + i \frac{e^2}{8\hbar m \omega^3} M - i \frac{e^2 F_1 F_2}{4\hbar m \omega^2} N \right], \quad x \geq 0, \end{aligned} \quad (\text{A3b})$$

when $F_0 \neq 0$, where $E_l = \varepsilon + l\hbar\omega - V_0 - U_{p1} - U_{p2}$ with $V_0 = W_{\text{eff}} + E_F$ and ponderomotive energy $U_{p1} = \frac{e^2 F_1^2}{4m\omega^2}$ and $U_{p2} = \frac{e^2 F_2^2}{16m\omega^2}$ due to fundamental and second-harmonic fields, respectively, $L = \frac{eF_1 \sin \omega t}{\omega} + \frac{eF_2 \sin(2\omega t + \theta)}{2\omega}$, $M = F_1^2 \sin 2\omega t + \frac{F_2^2}{8} \sin[2(2\omega t + \theta)]$, $N = \frac{\sin(\omega t + \theta)}{\omega} - \frac{\sin(3\omega t + \theta)}{3\omega}$, $\eta_l = (\frac{2meF_0}{\hbar^2})^{1/3} (\xi + \frac{E_l}{eF_0})$ with $\xi = x + \frac{eF_1 \cos \omega t}{m\omega^2} + \frac{eF_2 \cos(2\omega t + \theta)}{4m\omega^2}$, Ai and Bi are the Airy function of the first and second kind, and T_l is the transmission coefficient.

Applying boundary conditions that $\psi(x, t)$ and $\partial\psi(x, t)/\partial x$ are continuous at the metal-vacuum interface $x = 0$, we obtain the following relationship:

$$2k_0 \delta(s) = \sum_{l=-\infty}^{\infty} T_l [k_s P_{l(l-s)} + Q_{l(l-s)}]. \quad (\text{A4})$$

Here, δ is Dirac delta function, $P_{l(l-s)} = (1/2\pi) \int_0^{2\pi} p_l(\omega t) e^{-i(l-s)\omega t} d(\omega t)$ and $Q_{l(l-s)} = (1/2\pi) \int_0^{2\pi} q_l(\omega t) e^{-i(l-s)\omega t} d(\omega t)$ are the $(l-s)$ th Fourier transform coefficients of $p_l(\omega t)$ and $q_l(\omega t)$ respectively:

$$\begin{aligned} p_l(\omega t) = & \exp \left[i \sqrt{\frac{2mE_l}{\hbar^2}} \left(\frac{eF_1 \cos \omega t}{m\omega^2} + \frac{eF_2 \cos(2\omega t + \theta)}{4m\omega^2} \right) \right] \\ & \times \exp \left[i \frac{e^2}{8\hbar m \omega^3} M - i \frac{e^2 F_1 F_2}{4\hbar m \omega^2} N \right], \end{aligned} \quad (\text{A5a})$$

$$q_l(\omega t) = \left[\sqrt{\frac{2mE_l}{\hbar^2}} + \frac{L}{\hbar} \right] p_l(\omega t), \quad (\text{A5b})$$

when $F_0 = 0$, and

$$p_l(\omega t) = [Ai(-\alpha_l) - iBi(-\alpha_l)] \exp \left[-i \frac{e^2 F_0 F_1 \sin \omega t}{\hbar m \omega^3} \right]$$

$$\begin{aligned} & \exp \left[-i \frac{e^2 F_0 F_2 \sin(2\omega t + \theta)}{8\hbar m \omega^3} \right] \\ & \times \exp \left[i \frac{e^2}{8\hbar m \omega^3} M - i \frac{e^2 F_1 F_2}{4\hbar m \omega^2} N \right], \end{aligned} \quad (\text{A5c})$$

$$\begin{aligned} q_l(\omega t) = & \left[i \left(\frac{2meF_0}{\hbar^2} \right)^{1/3} [Ai'(-\alpha_l) - iBi'(-\alpha_l)] \right. \\ & \left. + \frac{L}{\hbar} [Ai(-\alpha_l) - iBi(-\alpha_l)] \right] \exp \left[-i \frac{e^2 F_0 F_1 \sin \omega t}{\hbar m \omega^3} \right. \\ & \left. - i \frac{e^2 F_0 F_2 \sin(2\omega t + \theta)}{8\hbar m \omega^3} \right] \\ & \times \exp \left[i \frac{e^2}{8\hbar m \omega^3} M - i \frac{e^2 F_1 F_2}{4\hbar m \omega^2} N \right] \end{aligned} \quad (\text{A5d})$$

when $F_0 \neq 0$, where $\alpha_l = \eta_l(x = 0)$.

With the electron transmission coefficient T_l solved from Eq. (A4), the time-averaged probability of electron transmission from initial energy of ε through the l -photon process is given as

$$w_l(\varepsilon) = \begin{cases} \frac{1}{k_0} \text{Im} \left[i \sqrt{\frac{2m}{\hbar^2}} E_l |T_l|^2 \right], & F_0 = 0 \\ \frac{1}{k_0} \left(\frac{2meF_0}{\hbar^2} \right)^{1/3} \frac{1}{\pi} |T_l|^2, & F_0 \neq 0 \end{cases} \quad (\text{A6})$$

and the total electron transmission probability for an initial energy of ε is a sum of w_l through all the l -photon processes, which is Eq. (2) in the main text.

- [1] X. Xie, S. Roither, D. Kartashov, E. Persson, D. G. Arbó, L. Zhang, S. Gräfe, M. S. Schöffler, J. Burgdörfer, A. Baltuška, and M. Kitzler, *Phys. Rev. Lett.* **108**, 193004 (2012).
 [2] V. Gruson, L. Barreau, Á. Jiménez-Galan, F. Risoud, J. Caillat, A. Maquet, B. Carré, F. Lepetit, J.-F. Hergott, T. Ruchon,

- L. Argenti, R. Taïeb, F. Martín, and P. Salières, *Science* **354**, 734 (2016).
 [3] M. Förster, T. Paschen, M. Krüger, C. Lemell, G. Wächter, F. Libisch, T. Madlener, J. Burgdörfer, and P. Hommelhoff, *Phys. Rev. Lett.* **117**, 217601 (2016).
 [4] S. K. Cushing, *Nat. Photonics* **11**, 748 (2017).

- [5] Y. Luo and P. Zhang, *Phys. Rev. B* **98**, 165442 (2018).
- [6] Y. Luo and P. Zhang, *Phys. Rev. Applied* **12**, 044056 (2019).
- [7] A. G. Joly, P. Z. El-Khoury, and W. P. Hess, *J. Phys. Chem. C* **122**, 20981 (2018).
- [8] B. Ji, X. Song, Y. Dou, H. Tao, X. Gao, Z. Hao, and J. Lin, *New J. Phys.* **20**, 073031 (2018).
- [9] Z. Zhao, P. Lang, Y. Qin, B. Ji, X. Song, X. Song, J. Lin, and J. Lin, *Opt. Express* **28**, 19023 (2020).
- [10] T. Paschen, C. Nauk, P. Dienstbier, and P. Hommelhoff, *J. Phys. B: At. Mol. Opt. Phys.* **54**, 144006 (2021).
- [11] P. Dienstbier, T. Paschen, and P. Hommelhoff, *Nanophotonics* **10**, 3717 (2021).
- [12] J. Tan, Y. Zhou, M. He, Y. Chen, Q. Ke, J. Liang, X. Zhu, M. Li, and P. Lu, *Phys. Rev. Lett.* **121**, 253203 (2018).
- [13] Y. Li, Y. Yang, C. Qin, Y. Song, S. Han, G. Zhang, R. Chen, J. Hu, L. Xiao, and S. Jia, *Phys. Rev. Lett.* **127**, 073902 (2021).
- [14] A. H. Zewail, *Science* **328**, 187 (2010).
- [15] E. Najafi, T. D. Scarborough, J. Tang, and A. Zewail, *Science* **347**, 164 (2015).
- [16] A. Feist, N. Bach, N. Rubiano da Silva, T. Danz, M. Möller, K. E. Priebe, T. Domröse, J. G. Gatzmann, S. Rost, J. Schauss, S. Strauch, R. Bormann, M. Sivilis, S. Schäfer, and C. Ropers, *Ultramicroscopy* **176**, 63 (2017).
- [17] S. Sun, X. Sun, D. Bartles, E. Wozniak, J. Williams, P. Zhang, and C.-Y. Ruan, *Struct. Dyn.* **7**, 064301 (2020).
- [18] P. Hommelhoff, Y. Sortais, A. Aghajani-Talesh, and M. A. Kasevich, *Phys. Rev. Lett.* **96**, 077401 (2006).
- [19] C. Pellegrini, *Phys. Scr.* **T169**, 014004 (2016).
- [20] B. Piglosiewicz, S. Schmidt, D. J. Park, J. Vogelsang, P. Groß, C. Manzoni, P. Farinello, G. Cerullo, and C. Lienau, *Nat. Photonics* **8**, 37 (2014).
- [21] Y. Yang, M. Turchetti, P. Vasireddy, W. P. Putnam, O. Karnbach, A. Nardi, F. X. Kärtner, K. K. Berggren, and P. D. Keathley, *Nat. Commun.* **11**, 3407 (2020).
- [22] Y. Luo, Y. Zhou, and P. Zhang, *Phys. Rev. B* **103**, 085410 (2021).
- [23] E. Forati, T. J. Dill, A. R. Tao, and D. Sievenpiper, *Nat. Commun.* **7**, 13399 (2016).
- [24] P. Zhang, A. Valfells, L. K. Ang, J. W. Luginsland, and Y. Y. Lau, *Appl. Phys. Rev.* **4**, 011304 (2017).
- [25] X. Xiong, Y. Zhou, Y. Luo, X. Li, M. Bosman, L. K. Ang, P. Zhang, and L. Wu, *ACS Nano* **14**, 8806 (2020).
- [26] P. Zhang, Y. S. Ang, A. L. Garner, Á. Valfells, J. W. Luginsland, and L. K. Ang, *J. Appl. Phys.* **129**, 100902 (2021).
- [27] P. Lang, B. Ji, X. Song, Y. Dou, H. Tao, X. Gao, Z. Hao, and J. Lin, *Opt. Lett.* **43**, 5721 (2018).
- [28] Y. Luo and P. Zhang, *Appl. Phys. Lett.* **119**, 194101 (2021).
- [29] T. Paschen, M. Förster, M. Krüger, C. Lemell, G. Wächter, F. Libisch, T. Madlener, J. Burgdörfer, and P. Hommelhoff, *J. Mod. Opt.* **64**, 1054 (2017).
- [30] W. Cheng-Wei Huang, M. Becker, J. Beck, and H. Batelaan, *New J. Phys.* **19**, 023011 (2017).
- [31] A. Li, Y. Pan, P. Dienstbier, and P. Hommelhoff, *Phys. Rev. Lett.* **126**, 137403 (2021).
- [32] P. Dienstbier, T. Paschen, and P. Hommelhoff, *J. Phys. B: At. Mol. Opt. Phys.* **54**, 134002 (2021).
- [33] Y. Luo, J. Luginsland, and P. Zhang, *AIP Adv.* **10**, 075301 (2020).
- [34] P. Zhang and Y. Y. Lau, *Sci. Rep.* **6**, 19894 (2016).
- [35] Y. Zhou and P. Zhang, *J. Appl. Phys.* **127**, 164903 (2020).
- [36] Y. Zhou and P. Zhang, *J. Appl. Phys.* **130**, 064902 (2021).
- [37] See Supplemental Material at <http://link.aps.org/supplemental/10.1103/PhysRevB.106.085402> for the discussion of transmission probability and visibility, prefactor fitting, and decomposed transmission probability.
- [38] C. Chen, Y.-Y. Yin, and D. S. Elliott, *Phys. Rev. Lett.* **64**, 507 (1990).
- [39] B. Sheehy, B. Walker, and L. F. DiMauro, *Phys. Rev. Lett.* **74**, 4799 (1995).
- [40] P. Dombi, Z. Pápa, J. Vogelsang, S. V. Yalunin, M. Sivilis, G. Herink, S. Schäfer, P. Groß, C. Ropers, and C. Lienau, *Rev. Mod. Phys.* **92**, 025003 (2020).
- [41] D. Novko, V. Despoja, M. Reutzler, A. Li, H. Petek, and B. Gumhalter, *Phys. Rev. B* **103**, 205401 (2021).
- [42] P. Zhang and Y. Y. Lau, *J. Plasma Phys.* **82**, 595820505 (2016).
- [43] Y. Luo and P. Zhang, *Phys. Rev. Applied* **17**, 044008 (2022).
- [44] S. Banerjee and P. Zhang, *J. Vac. Sci. Technol. A* **40**, 030802 (2022).
- [45] N. Shivaram, H. Timmers, X.-M. Tong, and A. Sandhu, *Phys. Rev. Lett.* **108**, 193002 (2012).
- [46] C. W. Hogle, X. M. Tong, L. Martin, M. M. Murnane, H. C. Kapteyn, and P. Ranitovic, *Phys. Rev. Lett.* **115**, 173004 (2015).
- [47] D. Kolbasova, M. Hartmann, R. Jin, A. Blättermann, C. Ott, S.-K. Son, T. Pfeifer, and R. Santra, *Phys. Rev. A* **103**, 043102 (2021).
- [48] Y. Wang and C. H. Greene, *Phys. Rev. A* **103**, 053118 (2021).
- [49] Y. Wang and C. H. Greene, *Phys. Rev. A* **105**, 013113 (2022).
- [50] W. S. Truscott, *Phys. Rev. Lett.* **70**, 1900 (1993).